

Synthetic Modeling of an Imaging Motional Stark Effect Diagnostic for Edge Current Density Measurements on MAST-U

S. Gibson,^{1,2} A. Thorman,² C. Michael,³ N. C. Hawkes,² M. Carr,² J. Howard,³ and R. M. Sharples¹

¹*Centre for Advanced Instrumentation, Durham University, Durham, DH1 3LE*

²*CCFE, Culham Science Centre, Abingdon, Oxon, OX14 3DB, UK*

³*Plasma Research Laboratory, Australian National University, Canberra, Australia*

The Motional Stark Effect (MSE) diagnostic is used to measure the magnetic pitch angle in fusion devices and constrain equilibrium reconstruction codes for inference of q and current j_ϕ profiles. An imaging MSE diagnostic was modeled and designed for MAST-U using the spectral modeling code MSESIM. Forward modeled images and synthetic 2D polarisation angle profiles were generated for a typical MAST H-mode plasma. The simulated polarisation angle γ profiles are resolved in the presence of shot noise with a standard deviation of $\sigma = \pm 0.5^\circ$ at 1ms exposure times.

INTRODUCTION

High confinement (H) mode plasmas are characterised by large gradients in temperature, pressure and current profiles within the plasma edge. Electron temperature T_e and density n_e measurements are routinely made in the pedestal region by the Thompson scattering (TS) diagnostic[1],[3], from which the pressure profile is derived. Normally the current density j_ϕ is neoclassically derived from the pressure gradient as there are few examples of diagnostics[4],[5],[6] which can routinely provide current profiles at high spatial and temporal resolution.

The motional Stark effect (MSE) diagnostic [7] measures the magnetic pitch angle $\gamma = \arctan(B_\theta/B_\phi)$, where B_θ is the poloidal and B_ϕ the toroidal magnetic field. MSE measurements are used as a radial constraint for equilibrium reconstruction, from which q and toroidal current j_ϕ profiles can be inferred. MSE diagnostics provide between 10-30 radial measurements of the pitch angle using fiber arrays, with a spatial resolution on MAST of $\Delta R = 2\text{-}3\text{cm}$ [8]. Measurements of j_ϕ have been made using MSE on MAST [4], however this analysis is dependent on the accuracy of the measured profiles and equilibrium reconstruction. The pedestal width on MAST is on the order of 2-3cm [9], which corresponds to 2-3 radial MSE channels around the pedestal region. Given that the toroidal current profile is calculated by taking spatial gradients of the magnetic field B , resolving an edge current peak with high accuracy is challenging.

The imaging motional Stark effect (IMSE) diagnostic[10] is a polarisation interferometer which captures 2D snapshot images of neutral beam emission. Polarisation information is encoded as an interference pattern in the image, which is generated using birefringent waveplates. IMSE provides high spatial resolution, 2D measurement of the pitch angle, which is particularly advantageous for constraining equilibrium reconstruction. Other physics

avenues which can be explored using this diagnostic include measuring edge pedestal structures[11] and q profile evolution[13].

A synthetic IMSE diagnostic has been designed and modeled for implementation on MAST-U. The *ab initio* model MSESIM[12] was used to model the MSE spectrum, which included realistic spectral broadening effects. Synthetic diagnostic images were produced; an ideal case without inclusion of systematic error, and a realistic case in which random shot noise and distortion due to non-axial ray effects were included. The synthetic images were demodulated to produce polarisation angle profiles which were compared to EFIT[2] and MSESIM. A 2D B_z profile was recovered from the image and compared to EFIT B_z contours.

CONVENTIONAL MSE

The MSE diagnostic measures Doppler shifted emission from neutral beam atoms, which experience a strong Lorentz electric $\mathbf{E} = \mathbf{V} \times \mathbf{B}$ field as they move through the non-uniform external magnetic field \mathbf{B} . The strong \mathbf{E} field induces Stark splitting of the energy levels, from which emission is polarised parallel (π) or perpendicular (σ) to the \mathbf{E} field. By measuring the polarisation angle γ one can determine the orientation of the Lorentz \mathbf{E} field and subsequently the magnetic pitch angle γ_{pitch} . A convenient notation used to describe polarised light is the stokes vector \mathbf{S} ,

$$\mathbf{S} = (S_0, S_1, S_2, S_3) = I_0(1, P_l \cos 2\gamma, P_l \sin 2\gamma, P_c) \quad (1)$$

where I_0 , and hence S_0 , is the total light intensity, P_l is the linear polarised fraction, P_c is the circular polarised fraction and γ is the polarisation angle.

To measure the pitch angle on conventional systems, the polarisation angle is encoded as an intensity modulation using photoelastic modulators (PEMs) and avalanche photodiodes (APDs). As the Doppler shifted wavelength

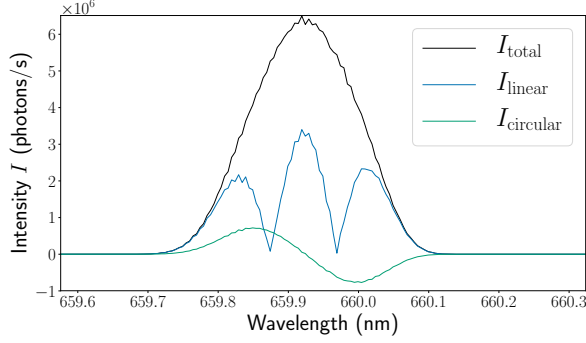


FIG. 1. The full energy component of the MSE spectrum on MAST, modeled using MSESIM. Stark split π and σ components are shown in blue, though these can only be resolved experimentally at high magnetic fields and beam energies.

of the emission depends heavily on the line of sight, each viewing chord requires a specific narrowband interference filter in order to select either a π or σ line. A typical modeled MAST spectrum is shown in Fig.1 where the multiplet is resolved. On MAST-U the Stark wavelength splitting is weak due to the small \mathbf{B} field and so broadening effects dominate, such that the multiplet cannot be fully resolved experimentally[8].

Forward modeled MSE spectra is produced using the *ab initio* modeling code MSESIM[12]. MSESIM is a machine independent code that simulates realistic spectral broadening of the MSE multiplet. The code considers broadening effects due to the collection volume, viewing solid angle and beam velocity distribution and returns the emission intensity for each sight line, given as a stokes vector $\mathbf{S}(\lambda)$ and polarised fractions $P_l(\lambda)$ and $P_c(\lambda)$ as a function of wavelength. Further inclusions to the code have been made by P. Geelen[17] which focus on improvements in atomic modeling. Inclusion of the Stark-Zeeman states allows for the circular polarisation fraction to be calculated, which on MAST is around 9%. Other significant inclusions are line intensity ratios, which assume a non-statistical upper state population [14]. Non-statistical upper state populations occur in the stark-zeeman lines at low plasma gas densities. During beam into gas calibrations on MAST[8], it was observed that the π component was stronger than the σ component of the spectrum. Accurate modelling of the S_3 component using the stark-zeeman states and non-statistical upper state populations could lead to improved understanding of discrepancies between the expected and observed calibration spectra. For the purposes of producing synthetic spectrum for simulated diagnostic images in this paper, a magnetics EFIT equilibrium was used from MAST shot 18501 at $t=0.29$ s, which was a conventional divertor configuration, H mode plasma.

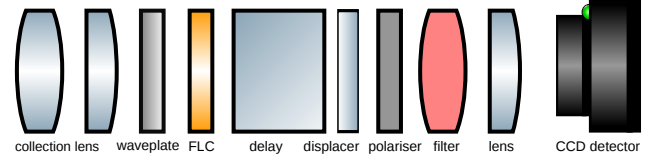


FIG. 2. Optical setup of the IMSE system, which includes a quarter waveplate with axis at $\rho=45^\circ$ to suppress sensitivity to the S_3 component. The FLC switching waveplate ($\rho=45^\circ/90^\circ$), a delay plate and displacer plate ($\rho=90^\circ$) which cause a phase shift between the ordinary and extraordinary components of the incident light. A polariser ($\rho=45^\circ$) recombines these components. The interference filter selects the MSE multiplet and the interference pattern is produced on an imaging CCD detector.

IMAGING MSE

A simple setup consists of linearly polarised light $\mathbf{S} = (S_0, S_1, S_2, 0)$ incident on a birefringent waveplate with its fast axis at 45° to a polariser, and an imaging detector. The waveplate introduces a phase delay ϕ between the ordinary and extraordinary components of the incident ray, which when recombined with a polariser produces an interference pattern where the intensity on the detector is given by,

$$I = \frac{1}{2}(S_0 + S_1 \cos \phi) = \frac{1}{2}I_0(1 + \cos 2\gamma \cos \phi) \quad (2)$$

The full IMSE system is shown in Fig.2. A quarter wave plate is included in front of the delay plate to encode the polarisation orientation as a phase modulation,

$$I = \frac{1}{2}(S_0 + S_1 \sin \phi - S_2 \cos \phi) = \frac{I_0}{2}(1 + \cos(\phi - 2\gamma)) \quad (3)$$

$$I = \frac{1}{2}(S_0 + S_1 \sin \phi + S_2 \cos \phi) = \frac{I_0}{2}(1 + \cos(\phi + 2\gamma)) \quad (4)$$

A ferroelectric crystal (FLC) waveplate is included, which when subjected to a voltage waveform switches the orientation of its fast axis between 45° and 90° on the order of tens of μ s, leading to two measurements of the stokes vector. By taking an image in each state of the FLC, the sum of the phase demodulated images reveals the total phase shift of the delay plates ϕ , whilst the difference reveals polarisation angle γ , shown in Fig.6.

The phase delay ϕ imposed on incident light by a uniaxial birefringent waveplate is given by[19],

$$\phi = \frac{2\pi L \Delta n(\lambda)}{\lambda} [-\cos^2 \Theta + \frac{y \sin 2\Theta}{\bar{n}f}] + \frac{1}{4\bar{n}^2 f^2} (3 - \cos 2\Theta)x^2 - ((3 \cos 2\Theta) - 1)y^2) \quad (5)$$

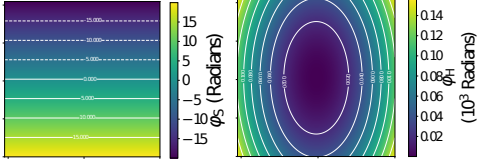


FIG. 3. Example of the linear ϕ_S and hyperbolic ϕ_H phase delay patterns produced using a displacer plate of $L=3\text{mm}$ and $\Theta=45^\circ$.

where L is the waveplate thickness $\Delta n(\lambda)$ is the birefringence, λ is the wavelength of the incident light, f is the focal length of the focusing lens, Θ is the cut angle of the optical axis, \bar{n} is the average of the ordinary and extraordinary refractive indices and x and y are the horizontal and vertical positions on the camera sensor. The phase delay can be split into three distinct terms, shown in Fig.3. The phase offset ϕ_0 , which is uniform across the crystal. A phase shear term ϕ_S imposes a vertical linear increase in phase across the crystal. Finally, a hyperbolic term ϕ_H is a higher order effect; it is dependent on the choice of lens focal length and camera sensor size.

IMSE Design for MAST-U

The total imposed phase delay acts as a sinusoidal filter over the spectrum and is chosen such that the delay matches the wavelength splitting of the multiplet. For MAST-U, the Stark wavelength splitting is $\delta\lambda=0.1\text{nm}$, meaning a phase delay on the order 10^4 waves must be applied, which can be achieved using thick birefringent waveplates. A displacer plate is also included in the system which has an optical axis at an angle Θ to the face of the crystal. This introduces the vertical linear ramp term ϕ_S in the phase delay across the crystal, allowing for tracking of the Doppler shifted emission across the beam.

The thickness of both the delay and displacer waveplates was chosen by maximizing the instrumental contrast ζ ,

$$\zeta(\lambda) = \frac{|S_0(\lambda) \exp(i\phi(\lambda))|}{S_0(\lambda)} \quad (6)$$

where S_0 is the total emission intensity and ϕ is the phase delay imposed by the waveplates. By performing a parameter scan over a range of waveplate thicknesses, shown in Fig.4, the optimum contrast is given using a delay plate of thickness 15mm with a displacer of thickness 3mm. Neglecting non-ideal effects such as deviations in crystal thickness, the contrast ranged from 60% in the core to 20% at the plasma edge. The emission intensity is weak in the core, however as the

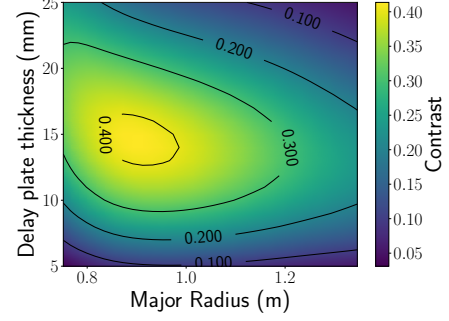


FIG. 4. The fringe contrast was calculated for a range of delay plate thicknesses. Optimum contrast was found using a delay plate of thickness $L=15\text{mm}$.

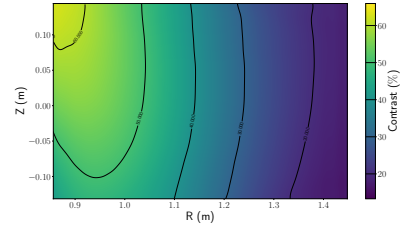


FIG. 5. 2D variation in fringe contrast ζ for an ideal delay plate $L=15\text{mm}$ and displacer plate $L=3\text{mm}$. The contrast is maximized in the plasma core and reaches a minimum of 20% at the plasma edge.

toroidal field B_ϕ is larger, the Stark splitting is more prominent and so line integration effects and broadening mechanisms have less of an effect on the contrast in the core than in the edge.

Variation in the cut angle of the optical axis Θ of the displacer crystal was also modeled. The choice of cut angle is important as it determines the carrier fringe frequency. If the frequency is too high, the vertical spatial resolution is limited. A cut angle $\Theta = 45^\circ$ was chosen to maximise the phase shear, whilst providing a fringe frequency of 13 pixels per fringe and minimal reduction of the fringe contrast.

A bandpass filter was designed to select the full energy component of the multiplet. However, an inherent issue with using bandpass filters in imaging systems is that the central wavelength of the filter varies with incident angle $\alpha = \frac{\sqrt{x^2+y^2}}{f}$ where x and y are the horizontal and vertical positions on the camera sensor, and f is the focal length of the camera lens. For the Photron SA-4 camera sensor with a lens of focal length $f=85\text{mm}$, $\alpha=6.87^\circ$.

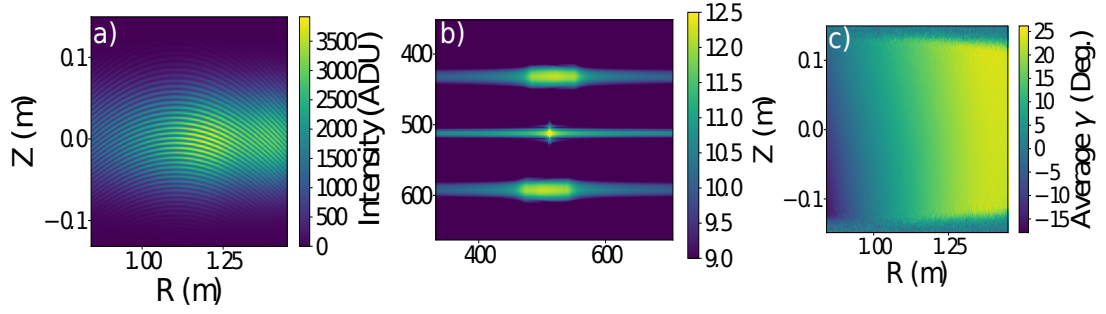


FIG. 6. Simulated noisy IMSE image (FLC polarisation = 45°) in figure a). Figure b) is the absolute value of the Fourier transform of the image on a logarithmic scale, showing the carrier frequency. Some low frequency broadband noise is present. The average 2D noisy polarisation angle γ profile in figure c) after applying shot noise and demodulating images over 100 times.

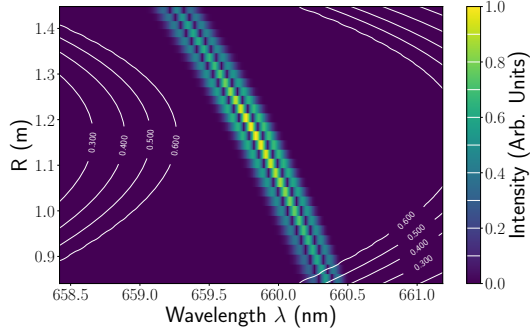


FIG. 7. Emission intensity of the full energy MSE multiplet as a function of wavelength λ and radius R . The transmission function of the designed bandpass filter is overlaid (white contours).

The bandpass center is shifted by,

$$\lambda_\alpha = \lambda_0 \sqrt{1 - \left(\frac{\sin \alpha}{n^*} \right)^2} \quad (7)$$

where λ_0 is the wavelength at normal incidence and n^* is the refractive index of the bandpass material. As the Doppler shift of the emission wavelength strongly depends on line of sight, the central wavelength shift effect can be used as an advantage when designing the bandpass filter. The focal length of the camera lens can be chosen such that the filter bandpass shift is in the same direction as the Doppler shift. The effect can be seen in Fig.7, where an $f=85\text{mm}$ focal length lens was chosen. Although at the extremities of the image, most prominently on the inboard side, vignetting of the image is apparent. The chosen bandpass filter was a 3nm FWHM filter, with a central wavelength $\lambda_{\text{cwl}}=660.5\text{nm}$, which should provide reduction of vignetting effects for measurements at the plasma edge and avoid contaminant second and third beam energy components.

RESULTS

Noisy synthetic images, shown in Fig.6, were simulated by taking the output emission intensity from MSESIM and imposing the phase delay of the IMSE system using Eq.3 and Eq.4 to return the intensity I incident on the CCD in photons per second. Photon shot noise was simulated by random sampling of a Poisson distribution with a mean given by the count rate $\lambda = I\tau$ where $\tau=1\text{ms}$ is the exposure time. To measure inter-ELM evolution of the current profile, an exposure time of $\tau=1\text{ms}$ is required. Dark noise and read noise were included by sampling Gaussian distributions centered around the measured values for the camera. The images were then digitized according to the CCD sensitivity. Both images were demodulated, ie. bandpass filtering around the carrier frequency to extract the phase information, from which the polarisation angle γ is retrieved. The standard deviation in the measurement was found to be $\sigma=\pm 0.5^\circ$ at 1ms exposure time, which is equivalent to the current conventional system.

A 2D B_z profile was inferred using the measured γ profile in Eq., where B_ϕ is the toroidal B field calculated from EFIT. The inferred B_z contours vary from the EFIT B_z contours in Fig.9 as geometry coefficients which are normally obtained during physical calibration of the diagnostic were initially neglected. Future work to improve the agreement includes using the calibration code CALCAM[20] to perform a synthetic diagnostic calibration to give an estimate for the geometry coefficients. This will also be used to determine the maximum spatial resolution of the diagnostic.

CONCLUSION AND OUTLOOK

An imaging motional Stark effect diagnostic was designed for the MAST-U tokamak. The MSE spectrum was modeled using MSESIM which included realistic spectral broadening features. The spectrum was used to create

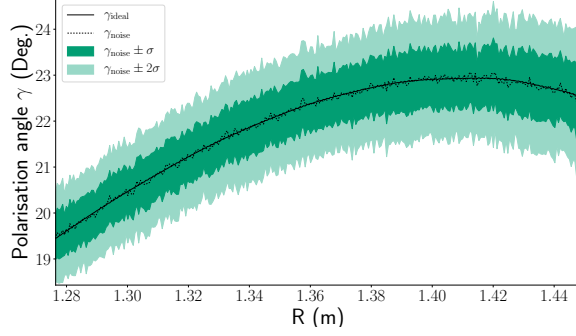


FIG. 8. A slice through the 2D polarisation angle γ shown in Fig.6 using ideal (no noise) images (solid black) compared to the average "noisy" profile (dashed black) calculated by demodulating noisy images including shot noise, dark noise and read noise. The filled regions show the average polarisation angle with confidence intervals of $\pm\sigma$ and $\pm2\sigma$. The profile is zoomed in to the edge of the plasma, as this is the region of interest for measuring edge currents.

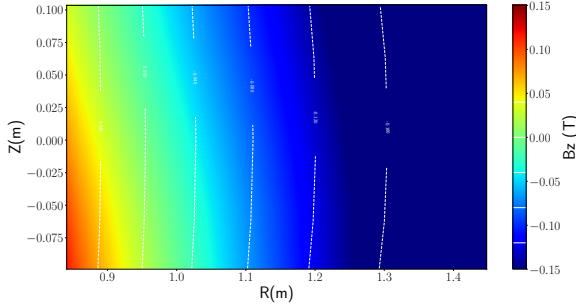


FIG. 9. 2D B_z profile derived from the simulated γ profile. Contours of the B_z profile calculated from EFIT are overlaid in white. Discrepancies in the shape of the contours are attributed to neglecting geometry coefficients which are normally obtained during diagnostic calibration.

synthetic diagnostic images which were demodulated to calculate the polarisation angle, which agreed with the MSESIM γ profile. The simulated measurements show that the proposed IMSE system would provide polarisation angle measurements with a standard deviation of $\sigma = \pm 0.5^\circ$ at an exposure time of 1ms. A 2D B_z profile was inferred using the γ profile, however the B_z contours did not align with those calculated using EFIT. This is likely due to neglecting geometry coefficients, however these can be calculated by performing a synthetic calibration of the diagnostic using a calibration code such as CALCAM. Next steps also include using a range of EFIT equilibrium with current profile shapes as an input to MSESIM, in order to determine the spatial resolution of the system and the accuracy to which edge current peaks can be detected. Improvement in accuracy of equilibrium reconstruction using the IMSE system as opposed to conventional MSE will be explored.

ACKNOWLEDGEMENTS

The author would like to thank Prof. John Howard and the Plasma Research Laboratory, ANU for financial assistance. This work was supported by the Engineering and Physical Sciences Research Council [EP/L01663X/1].

- [1] J. W. Hughes, D. A. Mossessian, A. E. Hubbard, and E. S. Marmar, *Rev. Sci. Instrum.*, **72**(1), (2001)
- [2] L. Lao, et al. *Nucl. Fusion*, **25**(11), (1985)
- [3] R. Scannell *Rev. Sci. Instrum.* **77**(10), (2006)
- [4] M. F. M. De Bock, J. Citrin, S. Saarelma, D. Temple, N. J. Conway, A. Kirk, H. Meyer, C. A. Michael, and the MAST team, *Plasma Phys. Control. Fusion*, **54**(2), (2012)
- [5] M.G. Dunne, P.J. McCarthy, E. Wolfrum, R. Fischer, L. Giannone, A. Burckhart and the ASDEX Upgrade Team, *Nucl. Fusion*, **52**(12), (2012)
- [6] R. G. L. Vann, K. J. Brunner, R. Ellis, G. Taylor, and D. A. Thomas, *Rev. Sci. Instrum.* **87**(11), (2016)
- [7] R. J. Fonck, G. M. Gammel, R. Kaita, H. W. Kugel, E. T. Powell, and D. W. Roberts, *Phys. Rev. Lett.* **63**(19), (1989)
- [8] N. J. Conway, M. F. M. De Bock, C. A. Michael, M. J. Walsh, P. G. Carolan, N. C. Hawkes, E. Rachlew, J. F. G. McCone, S. Shibaev, and G. Wearing, *Rev. Sci. Instrum.*, **81**(10), (2010).
- [9] H. Meyer, M.F.M De Bock, N.J. Conway, S.J Freethy, K. Gibson, J. Hiratsuka, A. Kirk, C.A. Michael, T. Morgan, R. Scannell, G. Naylor, S. Saarelma, A.N Saveliev, V.F. Shevchenko, W. Suttrop, D. Temple, R.G.L. Vann and the MAST and NBI teams,
- [10] J. Howard, *Plasma Phys. Control. Fusion*, **50**(12), (2008)
- [11] J. Howard, C. Michael, H. Chen, R. Lester, A. Thorman, J. Chung, *J. Instrum.*, **10**(9), (2015)
- [12] M. F. M. De Bock, N. J. Conway, M. J. Walsh, P. G. Carolan, and N. C. Hawkes, *Rev. Sci. Instrum* **79**, 10F524 (2008)
- [13] O. P. Ford, A. Burckhart, R. McDermott, T. Ptterich, R. C. Wolf, and ASDEX Upgrade Team, *Rev. Sci. Instrum.* **87**(11), (2016)
- [14] M. F. Gu. et al. *Journal of Physics B: Atomic, Molecular and Optical Physics* 41.9 (2008): 095701.
- [15] F. E. Veiras, L. I. Perez, M. T. Garea, *Applied Optics*, **49**(15) (2010)
- [16] A. Leonard, A.W. Leonard, A. Herrmann, K. Itami, J. Lingertat, A. Loarte, T.H. Osborne, W. Suttrop, *J. Nucl. Mater.*, **266**, (1999)
- [17] P. Geelen, S. Scott, R. Mumgaard, and M. De Bock, MIT internship report, (2012)
- [18] H. Y. Yuh, Massachusetts Institute of Technology Thesis, (2005)
- [19] A. Thorman, Australian National University Thesis, Plasma Research Laboratory, Australian National University, Canberra, (2018)
- [20] S. Silburn, CALCAM calibration software, <https://github.com/euratom-software/calcam>, Accessed 28th August 2018.